Chinese Chemical Letters 36 (2025) 109907

Contents lists available at ScienceDirect

Chinese Chemical Letters

journal homepage: www.elsevier.com/locate/cclet

Fluorine-doped $K_{0.39}Mn_{0.77}Ni_{0.23}O_{1.9}F_{0.1}$ microspheres with highly reversible oxygen redox reaction for potassium-ion battery cathode

Zhuangzhuang Zhang, Yaru Qiao, Jun Zhao, Dai-Huo Liu, Mengmin Jia, Hongwei Tang, Liang Wang, Dongmei Dai*, Bao Li*

Collaborative Innovation Center of Henan Province for Green Manufacturing of Fine Chemicals, Key Laboratory of Green Chemical Media and Reactions (Ministry of Education), School of Chemistry and Chemical Engineering, Henan Normal University, Xinxiang 453007, China

ARTICLE INFO

Article history:
Received 29 January 2024
Revised 27 February 2024
Accepted 17 April 2024
Available online 18 April 2024

Keywords:
Layered oxides
Cathode
TM-O bond
Potassium ion batteries
Anion-doping

ABSTRACT

Mn-rich layered oxides are appealing cathodes for potassium ion batteries (PIBs) in view of their comprehensive virtues such as low cost, high energy density and mature craftsmanship. However, the insufficient covalency between transition metal (TM) and O usually induces irreversible structural evolution and cation migration during repeated insertion and extraction of K^+, resulting in capacity loss, voltage fading and sluggish kinetics. Herein, an anion substitution strategy is proposed for a stable operation of layered oxide cathode by adjusting the valence electron layer structure between TM and O. The resultant strong TM−O skeleton can inhibit the occurrence of side effects derive from Ni^{4+} during the deep depotassium process, so as to achieve a gentle structural transition. Consequently, stable cycling performance of $K_{0.39}Mn_{0.77}Ni_{0.23}O_{1.9}F_{0.1}$ (KMNOF) cathode is achieved with 77% capacity retention over 350 cycles at 100 mA/g, yielding high discharge capacity 93.5 mAh/g at 20 mA/g and significantly improved rate capability of 50.1 mAh/g at 500 mA/g, whereas irreversible structural evolution and rapid capacity fade with KMNO cathode. Finally, *in situ*/*ex situ* characterizations and theoretical computations sheds light on the charge transfer and structure evolution mechanisms of KMNOF.

Nowadays, lithium-ion batteries (LIBs) become indispensable in our daily life as the main power source for electronics and electric vehicles [1,2]. However, the low reserves and high cost of lithium resource poses a bottleneck risk for development of LIBs [3,4]. Attracted by the abundant availability of potassium and low redox potential of K^+/K close to Li^+/Li (–2.93 V *vs.* –3.04 V), potassium-ion batteries (PIBs) have attracted extensive attention in recent years [5–7]. Nevertheless, the large size of K^+ (1.38 Å) could result in poor K^+-migration kinetics and large voltage hysteresis [8,9]. Meanwhile, the huge K^+ commonly brings about large crystal strain during insertion and extraction processes, thereby deteriorating the cycling stability of cathode materials. Therefore, it is vital to develop reasonable electrode materials with superior K^+ diffusion dynamics and structural stability.

In fact, cathode materials determine their power density and energy density of PIBs [10,11]. However, limited types of cathode materials have been developed, including layered transition metal oxides (TMOs) [12,13], phosphate compounds [14,15], organic materials [16] and Prussian blue analogues [17,18]. Among them, TMOs have received widespread investigations on account of their 2D diffusion pathway, large specific capacity and high redox potential, which is considered an ideal cathode material for potassium ion batteries [19,20]. In addition, the synthesis procedures of TMOs is simple and convenient, which would greatly reduce the synthesis cost and be suitable for large-scale production [21].

In terms of the TMOs, the implementation of diverse electrochemical features depends on the transition metals [22,23]. Mn-based layered transition metal oxides possess greater business prospects than Co, Cr and V-based oxides in K^+ storage owing to higher reversible capacity and natural abundance [24]. Layered $K_{0.3}MnO_2$ cathode was first reported by Vaalma *et al.* [25] and the potassium storage mechanism was demonstrated by Ceder and coworkers [26]. To suppress Mn^{3+} Jahn-Teller distortion, part of Mn is replaced by active or inactive elements (such as Fe, Ni, Co, Ti and Mg elements) to improve electrochemical performance [27–29]. Among them, Ni is often selected as the dopant in Mn-based layered oxides because the ionic radius of Ni^{2+} (0.69 Å) is similar to that of Mn^{3+} (0.645 Å). For example, Myung *et al.* doped Ni^{2+} into $K_{0.5}MnO_2$ to reduce the amount of Mn^{3+}, resulting in a first discharge capacity of about 121 mAh/g with 82% retention for 100 cycles [30]. Recently, Zhou *et al.* [31] reported a cocoon-like Mn-

* Corresponding authors.
E-mail addresses: daidongmei@htu.edu.cn (D. Dai), libao@htu.edu.cn (B. Li).

https://doi.org/10.1016/j.cclet.2024.109907
1001-8417/

based layered oxides for PIBs by a self-template method, which deliver a rate capability of 57.1 mAh/g at 500 mA/g and an improved cycling stability. Nonetheless, the sluggish transport kinetics of larger K-ion within cathode materials seriously reduces the power density of PIBs [32]. Worse still, the severe structure distortion of layered framework during charge and discharge, as well as side reactions with electrolyte, further deteriorate the potassium storage performance [33]. To tackle with these dilemmas, facile and scalable designs should be exploited to boost structure stability of layered transition metal oxides and reduce the side reactions.

Herein, a facile configuration optimization strategy has been designed for the rational synthesis fluorine-doped $K_{0.39}Mn_{0.77}Ni_{0.23}O_{1.9}F_{0.1}$ microspheres (denoted KMNOF). High electronegativity F^- not only improve K^+ transmission kinetics by diminishing diffusion energy barrier, but also effectively suppress the formation of Ni^{4+} at high potential dispensing with irreversible side effects. More importantly, the substitution of F^- on anion sites can enhance the covalence of TM-O bond, which is beneficial for inhibiting unfavorable phase transition of P3-O3, ensuring the structural stability of the cathode material. In view of this, the as-prepared KMNOF exhibits improved cycle stability with 77% capacity retention over 350 cycles and dominant rate performance of 50.1 mAh/g at 500 mA/g.

The bottom-up preparation strategy for the fluorine-doped $K_{0.39}Mn_{0.77}Ni_{0.23}O_{1.9}F_{0.1}$ microspheres is schematically shown in Fig. S1 (Supporting information). $Mn_{0.78}Ni_{0.22}CO_3$ with an average size of about 9 μm have been first prepared by solvothermal reaction as the initial template (Figs. S2a and b in Supporting information). XRD diffraction peak and energydispersive X-ray spectroscopy (EDX) analysis prove the chemical components of the as-prepared $Mn_{0.78}Ni_{0.22}CO_3$ (Figs. S2c and d in Supporting information). After pre oxidation in the air, the $Mn_{0.78}Ni_{0.22}CO_3$ microspheres are transformed into the spherical $Mn_{1.56}Ni_{0.44}O_3$ precursor with a large amount of mesopores as confirmed by Fig. S3 (Supporting information). After the second step calcination with KF at elevated temperature in O_2 atmosphere, fluorine-doped $K_{0.39}Mn_{0.77}Ni_{0.23}O_{1.9}F_{0.1}$ (denoted as KMNOF) was successfully synthesized. For comparison, $K_{0.43}Mn_{0.78}Ni_{0.22}O_2$ (denoted as KMNO) without F^- was also prepared using KOH instead of KF (Figs. S4a–c in Supporting information). Detailed synthesis processes of KMNOF and KMNO are described in the Experimental section.

XRD Rietveld refinement of KMNOF is shown in Fig. 1a, in which all the diffraction peaks can be indexed to a hexagonal P3 phase with *R3m* space group (Table S1 in Supporting information). Scanning electron microscopy (SEM) image shows that as-prepared KMNOF still maintains a spherical structure, but the surface roughness increases due to high crystallinity of primary particle (Fig. 1b and Figs. S4d–f in Supporting information). The interior of KMNOF microspheres is solid as confirmed by transmission electron microscopy (TEM) in Fig. 1c. The high-resolution TEM image can clearly observe the distance of 0.64 nm between adjacent layers corresponding to the (003) planes (Fig. 1d). The detailed atomic arrangements along the [010] zone axis can be clearly observed in the ABF-STEM image, agreeing with the P3-type atomic model (Fig. 1e). The HAADF-STEM image (Fig. 1f) shows that the measured layer spacing (0.64 nm) matches well with the HR-TEM results. Meanwhile, K, Mn, Ni, F and O elements show a similar homogeneous distribution over the entire area in EDX elemental mapping (Fig. 1g). The atomic and mass ratios of all elements in KMNOF and KMNO are exactly consistent with their molecular formula by EDX measurements and the ICP test (Fig. S5 and Table S2 in Supporting information). The elemental valence states and chemical environment of KMNOF microspheres are clarified by XPS as observed in Fig. S6 (Supporting information). The high-resolution Mn 2p XPS spectrum contains the Mn $2p_{3/2}$ and Mn $2p_{1/2}$ peaks (Fig. 1h), which further divided into four peaks [34]. Among them, the

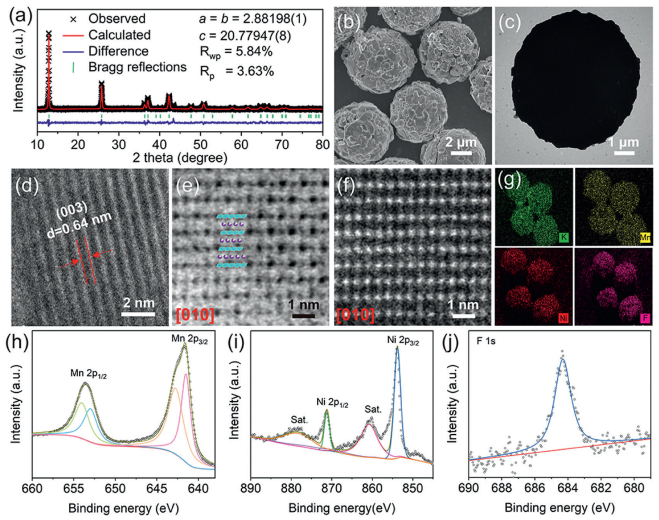

Fig. 1. (a) XRD Rietveld refinement, (b) SEM image, (c) TEM image and (d) HRTEM image of KMNOF. (e) ABF-STEM and (f) HAADF-STEM images of KMNOF along the [010] zone axis. (g) Scanning transmission electron microscopy images of KMNOF for K, Mn Ni and F elements. High-resolution XPS spectrum for (h) Mn 2p, (i) Ni 2p and (j) F 1s.

two peaks at 642.8 eV and 654.1 eV are assigned to Mn^{4+}, and the other two peaks at 641.5 eV and 652.9 eV arise from Mn^{3+}. In Fig. 1i, Ni 2p spectrum is composed of Ni $2p_{1/2}$ and Ni $2p_{3/2}$ along with their satellite peaks, meaning that the valence state of Ni is +2 [31]. Obviously, fluorinated TM bonds can be observed at 684.3 eV in the F 1s XPS spectrum, which indicates that O was successfully replaced by F (Fig. 1j) [21].

The potassium storage performance of the KMNOF and KMNO electrodes are investigated in K half cells. As shown in Fig. 2a, the electrochemical activity of KMNOF and KMNO cathodes are studied by cyclic voltammograms (CV) in first three cycles at a

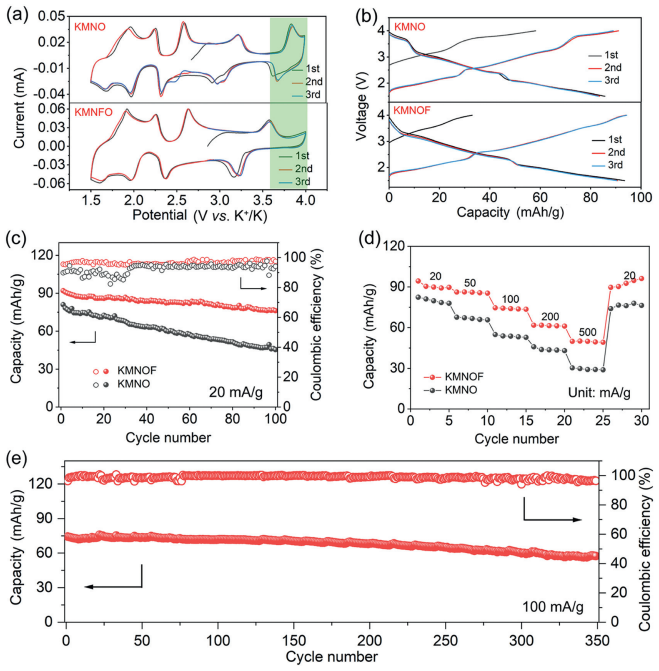

Fig. 2. (a) CV analysis at scan rate of 0.1 mV/s. (b) Galvanostatic charge/discharge profiles, (c) cycling performance and (d) rate capabilities of KMNOF and KMNO cathodes. (e) Long-term cyclic performance of KMNOF cathode at 100 mA/g.

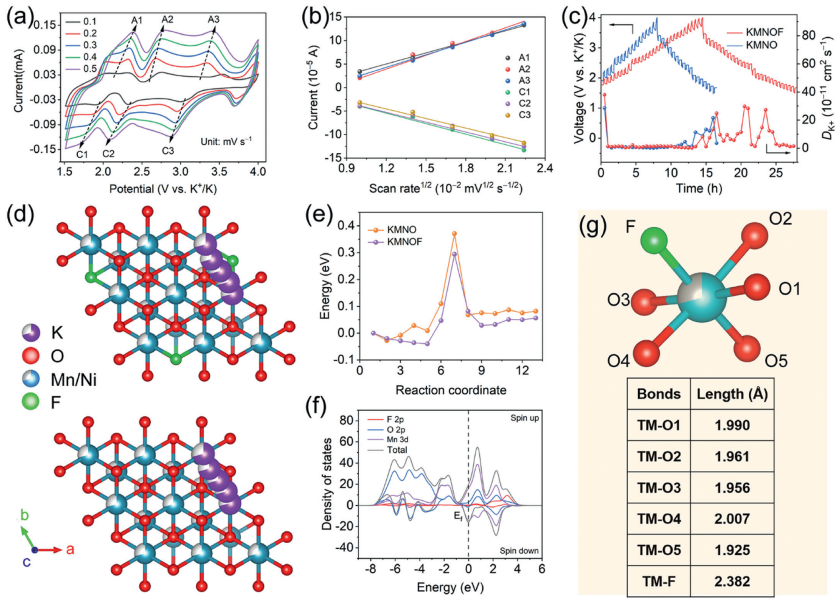

Bonds	Length (Å)
TM-O1	1.990
TM-O2	1.961
TM-O3	1.956
TM-O4	2.007
TM-O5	1.925
TM-F	2.382

Fig. 3. (a) CV curves from 0.1 mV/s to 0.5 mV/s and (b) the relevant linear fitting of KMNOF cathode. (c) GITT profiles and D_{K^+} of KMNOF and KMNO cathodes. (d) Calculated K^+ diffusion pathway and (e) K^+ migration energy barriers along the *ab* plane. (f) DOS of the KMNOF in the pristine status. (g) Schematic from the DFT calculation for Mn-O bonding distances of KMNOF.

sweep rate of 0.1 mV/s. The KMNO cathode indicate five pairs of redox peaks at 1.95/1.68 V, 2.25/1.97 V, 2.58/2.33 V, 3.22/2.98 V and 3.85/3.68 V. The first three pairs of redox peaks below 2.8 V can originate from the Mn^{4+}/Mn^{3+} redox pair and ordered structure of the K^+/vacancy [35]. In addition, according to the redox peaks at 3.22/2.98 V are assigned to Ni^{3+}/Ni^{2+} redox pair, particularly another pair of peaks at 3.85/3.68 V may be the Ni^{4+}/Ni^{3+} [36]. For the KMNOF, there are only four pairs of redox peaks located at 1.92/1.62 V, 2.26/1.98 V, 2.63/2.37 V and 3.58/3.23 V. Accordingly, the introduction of F can restrict the transition of Ni^{4+}/Ni^{3+}, and the redox pair of Ni^{3+}/Ni^{2+} also increases by 0.36 V. It is not difficult to find that the doped F is more inclined to replace the O around Ni due to the defect effect [37–39].

Fig. 2b, Figs. S7 and S8 (Supporting information) depict the charge/discharge profiles of KMNO and KMNOF electrodes in first three cycles. It is not surprising that the KMNO cathode presents a long voltage plateaus at 3.8–4.0 V, which becomes longer and longer during subsequent cycles (Fig. S9a in Supporting information), resulting in a decrease in Coulombic efficiency (CE). KMNOF cathode delivers a high discharge capacity of 93.5 mAh/g at 20 mA/g and subsequent curves are totally overlapped, showing the superior reversibility due to the introduction of F^- (Fig. S9b in Supporting information). After 100 cycles, the capacity retention KMNOF electrode can reach 83%, which is better than that of KMNO electrode (Fig. 2c). The rate capacities of KMNOF cathode are maintained at 90.2, 85.8, 74.1, 61.7, and 50.1 mAh/g at 20, 50, 100, 200, and 500 mA/g, respectively (Fig. 2d and Fig. S10 in Supporting information). When returning to 20 mA/g again, reversible capacity could restore to 92.7 mAh/g, indicating excellent tolerance of F^-doped structure towards rapid K^+ (de)intercalation. However, KMNO cathode without F only presents a lower capacity of 80.8, 66.7, 53.7, 43.3, and 29.5 mAh/g at 20–500 mA/g, respectively. Even at higher current density of 100 mA/g, a stable K de/intercalation can be detected over 350 cycles with 77% capacity retention (Fig. 2e).

The electrochemical kinetics of KMNOF cathode is measured by the CV examinations from 0.1 mV/s to 0.5 mV/s (Fig. 3a). The fitted lines for the anodic and cathodic peaks from above CV curves are depicted in Fig. 3b. According to the Randles–Sevcik equation [40], D_{K^+} (ion diffusion constant) of A1, C1, A2, C2, A3, and C3, are calculated to be 4.3×10^{-10}, 6.6×10^{-10}, 5.8×10^{-10}, 3.3×10^{-10}, 3.5×10^{-10}, and 4×10^{-10} cm^2/s. As a comparison, the D_{K^+} values of them for KMNO cathode are 4.1×10^{-10}, 3.3×10^{-10}, 2.5×10^{-10}, 3.5×10^{-10}, 4.5×10^{-10} and 2.4×10^{-10} cm^2/s (Fig. S11 in Supporting information), implying inferior K^+ migration speed than KMNOF. The subtle differences in potential responses for KMNOF and KMNO are further scrutinized by using GITT in Fig. 3c. Noticeably, the evolution of D_{K^+} values are all within the range of 10^{-10}–10^{-11} cm^2/s, in accord with the relevant results calculated of CV. Moreover, the first principles calculations reveal that KMNOF possess a minimum K^+ migration energy barrier of 0.29 eV in *ab* plane and wider ion transport channels (Figs. 3d and e, Fig. S12 in Supporting information), which rationalizes that KMNOF cathode exhibits improved rate capability over KMNO. The density of states (DOS) of KMNOF shows participation of F^- can effectively enhance the charge transfer of such a layered material (Fig. 3f and Fig. S13 in Supporting information). It is noteworthy that covalent TM−O bond has been significantly enhanced *via* the F-incorporating strategy, except for slight elongation in TM-O1 and TM-O4 (Fig. 3g and Table S3 in Supporting information).

In order to probe the potassium storage mechanism of KMNOF cathode upon cycling, *in-situ* XRD analysis are conducted during the concerned cycling profiles (Fig. 4a). During the charging process, the (003) and (006) peaks shift toward lower angles, revealing that interlayer distance is increasing along c-axis due to the large Coulombic repulsion of adjacent oxygen layers with extracting of K^+ (Fig. 4b) [41]. And then discharging from 4.0 V to 1.5 V, its (003) and (006) peaks gradually returns to higher angles, while new (101) and (102) peaks appears beside the original (101) and (102) peaks suggesting occurrence of a slight layer slip. When charging again from 1.5 V to 4.0 V, new (101) and (102) peaks can be restored to its original position. In the whole process, all the major diffraction peaks still belong to the P3-type hexagonal structure with *R3m* space group without characteristic peaks of other phase, such as O3 phase observed in the KMNO cathodes (Figs. S14 and S15 in Supporting information). Fig. 4c displays the evolution of lattice parameters of KMNOF derived from the *in situ* XRD results. Notably, the unit cell volume variation of KMNOF

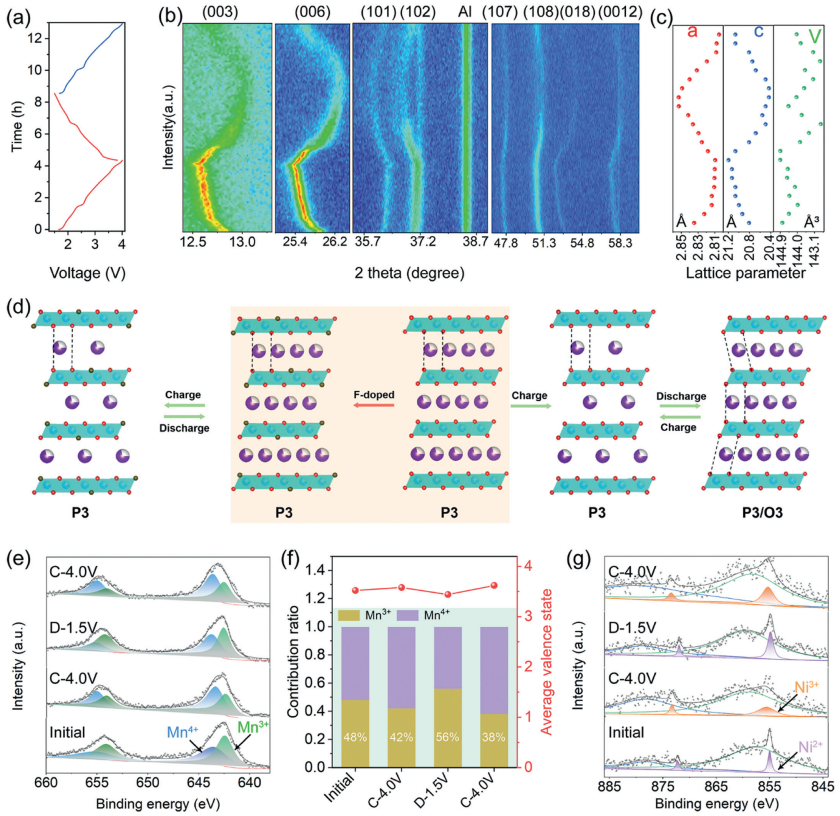

Fig. 4. (a) Typical charge/discharge curves of KMNOF cathode and (b) *in situ* XRD patterns. (c) Variation of cell volume calculated from XRD patterns. (d) Illustration of the structural evolution of KMNOF and KMNO upon cycling. *Ex situ* core-level XPS spectra of (e) Mn 2p and (g) Ni 2p. (f) Valence change of Mn calculated from (e).

is merely 1.4% during charge and discharge process. Such serious structure transformation caused by the weakened TM−O bond after cycling leads to the following drop of potassium storage sites and the blocked K^+ diffusion pathways, thus resulting in poor rate performance and cycling stability (Fig. 4d). For the KMNOF cathode, the formation of the robust O−TM−F configuration accounts for the reversible P3 structural evolution and rapid K^+ diffusivity.

To unveil the charge-transfer mechanism of KMNOF electrode materials, *ex-situ* XPS provides information on the valence state of manganese and nickel upon cycling. As diagrammatically drawn in Fig. 4e, the valence state of Mn remains a mixed valence state of +3 and +4 with proportional floating in the first charge and discharge. As calculation, the mean valance of Mn in the pristine KMNOF electrode is reckoned to be +3.52 (Fig. 4f). After charging to 4.0 V, a portion of Mn^{3+} ions are oxidized to Mn^{4+}, with an average valence of +3.58. Upon discharging to 1.5 V, the mean valance of Mn decreases to +3.44, while that returns to +3.62 during the subsequent charge process. Corresponding Ni 2p XPS spectra are elucidated in Fig. 4g. The Ni $2p_{1/2}$ (872.3 eV) and Ni $2p_{3/2}$ (854.9 eV) peaks of the pristine KMNOF electrode verify the bivalence of nickel. Upon charging to 4.0 V, the Ni $2p_{1/2}$ and Ni $2p_{3/2}$ peaks shift to higher binding energies of 873.3 and 855.8 eV, respectively, suggesting the entire oxidation of Ni^{2+} to Ni^{3+}. When discharging to 1.5 V, the peaks of Ni 2p return to the original position. The Ni $2p_{1/2}$ and Ni $2p_{3/2}$ peaks move toward a lower binding energy again upon recharging to 4.0 V, indicating the reversible redox of Ni^{2+}/Ni^{3+}.

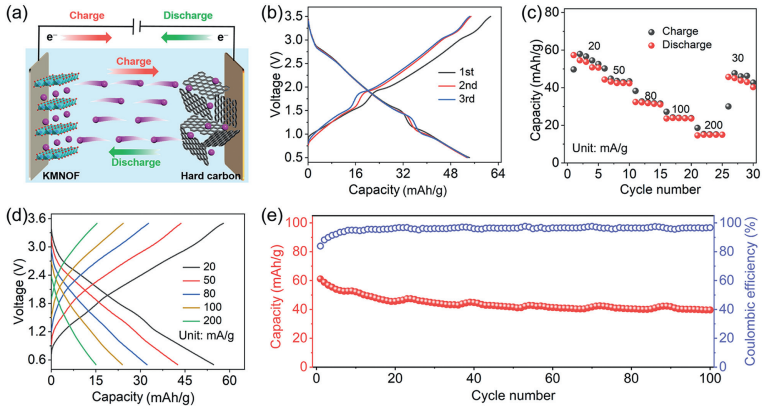

Fig. 5. (a) Schematic illustration of KMNOF//HC full batteries. (b) Galvanostatic charge–discharge profiles, (c) rate property and (d) corresponding charge–discharge profiles at varied current rates. (e) Cycling stability of K-ion full cell.

Hard carbon (HC) materials have been selected as anode electrodes to assemble into potassium ion full batteries with active mass ratio of 1:2.3 by matching as-obtained KMNOF cathode (Fig. 5a). The structural characterization and K-storage properties of HC anode is displayed in Figs. S16 and S17 (Supporting information). The voltage window of KMNOF//HC full batteries was set in 0.5−3.5 V. The initial charge and discharge capacities of the KMNOF//HC full cell are 61.5 and 54.3 mAh/g (based on the cathode) at 20 mA/g, respectively (Fig. 5b). The first three discharge curves almost overlap with multiple plateaus at 1.2, 1.5, and 3.8 V. Figs. 5c and d demonstrate the typical rate performance, which exhibits the reversible capacities of 53.8, 42.5, 31.8, 23.9, and 15.1 mAh/g at 20, 50, 80, 100, and 200 mA/g, respectively. The discharge capacity can be increased to 43.9 mAh/g when the current density is decreased back to 20 mA/g. Furthermore, such a full battery operates normally for 100 cycles with a capacity retention of 65% at 20 mA/g (Fig. 5e).

In summary, we demonstrated a viable structural optimization strategy by judiciously introducing high electronegativity F^- to craft Mn-rich layered cathodes improving diffusion kinetics and phase stability. Notably, the redox reaction of high potential Ni^{4+} is effectively inhibited through the lattice control of F, which helps reduce irreversible side effects during charge and discharge. In addition, the introduction of F that triggers the strong covalent TM−O bonds is critical to accelerate ion/electron transfer and stable configuration, and thus yielding better rate performance and cycling stability compared to KMNO without F doping. To explore the feasibility of application, a KMNOF//HC full battery was successfully assembled by using the hard carbon as an anode material, which also delivers a satisfactory cycling stability with 65% capacity retention after 100 cycles.

Declaration of competing interest

The authors declare that they have no known competing financial interests or personal relationships that could have appeared to influence the work reported in this paper.

Acknowledgments

This work was financially supported by the National Natural Science Foundation of China (No. 51902090), Henan Key Research Project Plan for Higher Education Institutions (No. 24A150019), and the Doctoral Start-Up Foundation (No. QD2022017).

Supplementary materials

Supplementary material associated with this article can be found, in the online version, at doi:10.1016/j.cclet.2024.109907.

References

[1] Y. Tian, G. Zeng, A. Rutt, et al., Chem. Rev. 21 (2021) 1623–1669.
[2] P.K. Nayak, L.T. Yang, W. Brehm, P. Adelhelm, Angew. Chem. Int. Ed. 57 (2018) 102–120.
[3] D. Zhou, D. Shanmukaraj, A. Tkacheva, M. Armand, G.X. Wang, Chem 5 (2019) 2326–2352.
[4] F. Ding, C. Zhao, D. Xiao, et al., J. Am. Chem. Soc. 144 (2022) 8286–28295.
[5] H.J. Liang, Z.Y. Gu, X.X. Zhao, et al., Sci. Bull. 67 (2022) 1581–1588.
[6] Z. Zhang, Y. Qiao, Q. Deng, et al., Inorg. Chem. Front. 10 (2023) 1286–1293.
[7] W. Luo, Y. Feng, D. Shen, et al., ACS Appl. Mater. Interfaces 14 (2022) 16379–16385.
[8] X. Lian, Z. Sun, Q. Mei, et al., Energy Environ. Mater. 5 (2022) 344–352.
[9] A. Li, Y. Man, J. Liao, et al., Nano Lett. 23 (2023) 10066–10073.
[10] A. Zhao, T. Yuan, P. Li, et al., Nano Energy 91 (2022) 106680.
[11] Q. Shi, R. Qi, X. Feng, et al., Nat. Commun. 13 (2022) 3205.
[12] Z. Zhang, J. Sun, L. Duan, et al., J. Mater. Chem. A 10 (2022) 554–560.
[13] S. Li, L. Wu, H. Fu, et al., Small Methods 7 (2023) 2300893.
[14] J. Liao, C. Chen, Q. Hu, et al., Angew. Chem. Int. Ed. 60 (2021) 25575–25582.
[15] J. Han, G.N. Li, F. Liu, et al., Chem. Commun. 53 (2017) 1805–1808.
[16] J. Duan, W. Wang, D. Zou, et al., ACS Appl. Mater. Interfaces 14 (2022) 31234–31244.
[17] H. Zhang, Y. Gao, J. Peng, et al., Angew. Chem. Int. Ed. 62 (2023) e202303953.
[18] X. Li, T. Guo, Y. Shang, et al., Adv. Mater. 36 (2024) 2310428.
[19] R.J. Luo, X.L. Li, J.Y. Ding, et al., Energy Storage Mater. 47 (2022) 408–414.
[20] Y.S. Xu, Y.N. Zhou, Q.H. Zhang, et al., Chem. Eng. J. 412 (2021) 128735.
[21] Y.S. Xu, M.Y. Qi, Q.H. Zhang, et al., ACS Appl. Mater. Interfaces 14 (2022) 13379–13387.
[22] Z. Zhang, L. Duan, A. Li, et al., Chem. Eur. J. 28 (2022) e202201562.
[23] F. Ding, H. Wang, Q. Zhang, et al., J. Am. Chem. Soc. 145 (2023) 13592–13602.
[24] M.G.T. Nathan, H. Yu, G.T. Kim, et al., Adv. Sci. 9 (2022) 2105882.
[25] C. Vaalma, G.A. Giffin, D. Buchholz, S. Passerini, J. Electrochem. Soc. 163 (2016) A1295–A1299.
[26] H. Kim, D.H. Seo, J.C. Kim, et al., Adv. Mater. 29 (2017) 1702480.
[27] X. Wang, X. Xu, C. Niu, et al., Nano Lett. 17 (2017) 544–550.
[28] J.U. Choi, J. Kim, J.Y. Hwang, et al., Nano Energy 61 (2019) 284–294.
[29] J. Weng, J. Dian, C. Sun, et al., Chem. Eng. J. 392 (2020) 123649.
[30] M.K. Cho, J.H. Jo, J.U. Choi, S.T. Myung, ACS Appl. Mater. Interfaces 11 (2019) 27770–27779.
[31] L. Duan, J. Xu, Y. Xu, et al., J. Energy Chem. 76 (2023) 332–338.
[32] J.U. Choi, J. Kim, J.H. Jo, et al., Energy Storage Mater. 25 (2020) 714–723.
[33] T. Deng, X. Fan, J. Chen, et al., Adv. Funct. Mater. 28 (2018) 1800219.
[34] J. Jin, Y. Liu, X. Zhao, et al., Angew. Chem. Int. Ed. 62 (2023) e202219230.
[35] Z. Xiao, F. Xia, L. Xu, et al., Adv. Funct. Mater. 32 (2022) 2108244.
[36] X. Zhang, Y. Yang, X. Qu, et al., Adv. Funct. Mater. 29 (2019) 1905679.
[37] X. Cui, S. Wang, X. Ye, et al., Energy Storage Mater. 45 (2022) 1153–1164.
[38] W.J. Shi, Y.W. Yan, C. Chi, et al., J. Power Sources 427 (2019) 129–137.
[39] S.B. Kim, H. Kim, D.H. Park, et al., J. Power Sources 506 (2021) 230219.
[40] M. Jiang, D.L. Danilov, R.A. Eichel, P.H.L. Notten, Adv. Energy Mater. 11 (2021) 2103005.
[41] Y. Wang, X. Zhao, J. Jin, et al., J. Am. Chem. Soc. 145 (2023) 22708–22719.